

Pamidronate functionalized nanoconjugates for targeted therapy of focal skeletal malignant osteolysis

Qian Yin^{a,1}, Li Tang^{a,1}, Kaimin Cai^a, Rong Tong^a, Rachel Sternberg^b, Xujuan Yang^c, Lawrence W. Dobrucki^d, Luke B. Borst^e, Debra Kamstock^f, Ziyuan Song^a, William G. Helferich^c, Jianjun Cheng^{a,2}, and Timothy M. Fan^{b,2}

^aDepartment of Materials Science and Engineering, University of Illinois at Urbana–Champaign, Urbana, IL 61801; ^bDepartment of Veterinary Clinical Medicine, University of Illinois at Urbana–Champaign, Urbana, IL 61801; ^cDepartment of Food Science and Human Nutrition, University of Illinois at Urbana–Champaign, Urbana, IL 61801; ^dDepartment of Bioengineering, University of Illinois at Urbana–Champaign, Urbana, IL 61801; ^eDepartment of Population Health and Pathobiology, North Carolina State University, Raleigh, NC 27606; and ^fDepartment of Environmental and Radiological Health Sciences, Colorado State University, Fort Collins, CO 80523

Edited by Omid C. Farokhzad, Brigham and Women's Hospital, Harvard Medical School, Boston, MA, and accepted by Editorial Board Member Mark E. Davis June 13, 2016 (received for review March 1, 2016)

Malignant osteolysis associated with inoperable primary bone tumors and multifocal skeletal metastases remains a challenging clinical problem in cancer patients. Nanomedicine that is able to target and deliver therapeutic agents to diseased bone sites could potentially provide an effective treatment option for different types of skeletal cancers. Here, we report the development of polylactide nanoparticles (NPs) loaded with doxorubicin (Doxo) and coated with bone-seeking pamidronate (Pam) for the targeted treatment of malignant skeletal tumors. In vivo biodistribution of radiolabeled targeted Pam-NPs demonstrated enhanced bone tumor accumulation and prolonged retention compared with nontargeted NPs. In a murine model of focal malignant osteolysis, Pam-functionalized, Doxo-loaded NPs (Pam-Doxo-NPs) significantly attenuated localized osteosarcoma (OS) progression compared with nontargeted Doxo-NPs. Importantly, we report on the first evaluation to our knowledge of Pam-Doxo-NPs in dogs with OS, which possess tumors of anatomic size and physiology comparable to those in humans. The repeat dosing of Pam-Doxo-NPs in dogs with naturally occurring OS indicated the therapeutic was well tolerated without hematologic, nonhematologic, and cardiac toxicities. By nuclear scintigraphy, the biodistribution of Pam-Doxo-NPs demonstrated malignant bone-targeting capability and exerted measurable anticancer activities as confirmed with percent tumor necrosis histopathology assessment.

focal skeletal malignant osteolysis | nanoconjugate drug delivery | large mammalian tumor model | osteosarcoma targeted therapy | canine comparative oncology

Malignant osteolysis associated with inoperable primary bone tumors and multifocal skeletal metastases remains a clinical challenge in cancer patients (1–3). Due to the progressive growth of osteotropic solid tumors, patients endure substantial morbidity consequent to the development of pathologic fracture and unrelenting bone pain (4–6). Effective therapies for treating malignant osteolysis include ionizing radiation, which exerts activity through the induction of tumor cell and osteoclast apoptosis within the diseased bone microenvironment (7–10). Additional adjuvant therapies combined with ionizing radiation can improve disease control and include systemic chemotherapies, small-molecule inhibitors, and anti-resorptive agents (11, 12). Despite the clinical institution of aggressive multimodality therapies, the outgrowth of residual cancer cells within the bone microenvironment is frequent, resulting in disease progression and treatment failure (13). As such, the discovery and validation of novel strategies, in particular targeted therapy, for treating osteotropic solid tumors is clinically warranted and necessary for improving long-term outcomes and survivorship with reduced side effects in cancer patients.

Nanomedicine that is able to deliver therapeutic agents to diseased sites could be an effective and complementary adjuvant treatment for inoperable focal and multifocal skeletal malignancies (14, 15). Nanoparticles (NPs) can be engineered to carry various

therapeutic agents, extravasate leaky blood vessels, reach and accumulate at tumor tissues, target malignant cancer cells, and release cargos in a controlled manner (16). When combined with active targeting ligands (e.g., antibodies, peptides, aptamers, or small molecules) NPs could be selectively targeted to specific tissues to treat certain types of cancer (17, 18). Targeted NPs hold great promise for minimizing systemic toxicity and improving therapeutic effectiveness against isolated tumor cell populations within skeletal niches (19–22). However, the clinical evaluation of promising nanotechnologies has been constrained to their evaluation in artificial preclinical rodent models systems, and the clinical advancement of promising nanotechnologies as superior treatment options for cancer patients suffering from malignant osteolysis has yet to be realized.

The translation of novel treatment strategies to clinical practice for improving the management of cancer-associated skeletal pathologies might be accelerated through the use of appropriate large mammalian tumor models that more closely recapitulate the processes involved in malignant osteolysis. Osteosarcoma (OS) is a solid tumor that causes severe focal bone destruction and is the most common primary bone tumor occurring in children and adolescents, accounting for ~60% of primary malignant bone

Significance

Malignant osteolysis associated with inoperable primary bone tumors and multifocal skeletal metastases remains a challenging clinical problem in cancer patients. The outgrowth of residual cancer cells within the bone microenvironment despite aggressive multimodality therapies necessitates the discovery and validation of novel strategies for treating osteotropic solid tumors. We report on pamidronate functionalized polylactide nanoparticles for the targeted treatment of focal malignant osteolysis by delivering doxorubicin specifically to the bone tumor microenvironment. Improved efficacy was demonstrated in a preclinical orthotopic mouse model of osteosarcoma. Most importantly, through the inclusion of dogs with naturally developing osteosarcoma, biocompatibility, biodistribution, and anticancer activities at clinically relevant dosages were demonstrated in a large mammalian modeling system.

Author contributions: Q.Y., L.T., R.T., J.C., and T.M.F. designed research; Q.Y., L.T., K.C., R.T., R.S., X.Y., L.W.D., and Z.S. performed research; X.Y., L.W.D., and W.G.H. contributed new reagents/analytic tools; Q.Y., L.T., K.C., R.T., R.S., X.Y., L.W.D., L.B.B., D.K., and T.M.F. analyzed data; and Q.Y., L.T., J.C., and T.M.F. wrote the paper.

The authors declare no conflict of interest.

This article is a PNAS Direct Submission. O.C.F. is a guest editor invited by the Editorial Board.

¹Q.Y. and L.T. contributed equally to this work.

²To whom correspondence may be addressed. Email: jianjunc@illinois.edu or t-fan@illinois.edu.

This article contains supporting information online at www.pnas.org/lookup/suppl/doi:10.1073/pnas.1603316113/-DCSupplemental.

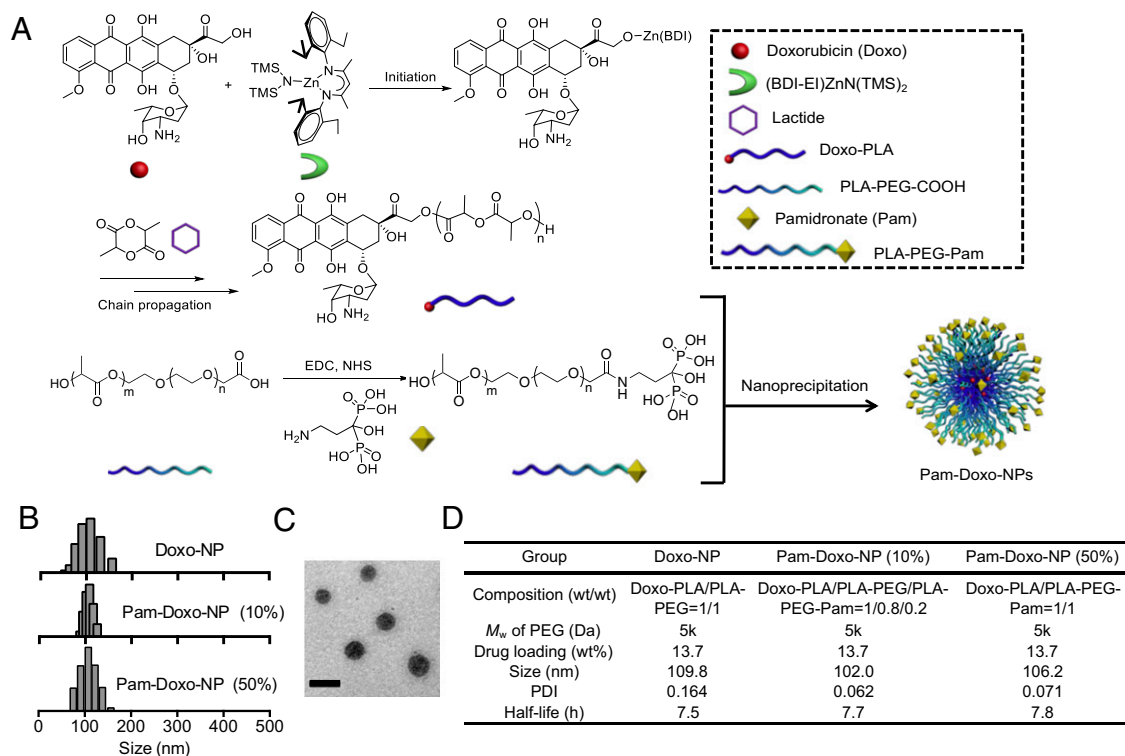


Fig. 1. Preparation and characterization of Pam-Doxo-NPs. (A) Schematic illustration of formulating Pam-Doxo-NPs. (B) Hydrodynamic sizes of NPs analyzed by DLS analysis. (C) TEM image of Pam-Doxo-NPs (50%) (Scale bar: 100 nm.) (D) Formulation parameters and physicochemical properties of Pam-Doxo-NPs and Doxo-NPs (*M_w* of PEG: molecular weight of PEG).

tumors diagnosed in the first two decades of life (23). Dogs spontaneously develop OS with the highest frequency of all mammal species; OS commonly affects older dogs of large or giant skeletal size (24). Biological, histological, and genomic features of OS in humans and dogs are highly similar and have provided a basis to evaluate novel therapeutics in dogs with OS (25–29). In addition, given the comparable anatomic size of humans and dogs (50 kg or greater) afflicted with OS, dogs might serve as more predictive models for comparable human pathologies based upon allometric scale similarities. Given these desirable modeling attributes and as part of the broader field of comparative oncology, translational drug development studies in dogs with OS have been used successfully to define dose and schedule for investigational therapeutic agents intended for development and clinical application in humans (30, 31).

Herein, we report a pamidronate (Pam) functionalized, polylactide (PLA)-based NP for the targeted treatment of focal malignant osteolysis by delivering doxorubicin (Doxo) specifically to the bone tumor microenvironment. Pam, a commonly used bisphosphonate, has been recognized for its excellent osteotropicity due to its exceptionally high affinity toward hydroxyapatite (HA), a major inorganic component of bone. The combination of active bone targeting mediated by Pam and passive tumor targeting through the enhanced permeation and retention (EPR) effect of NPs (32, 33) resulted in markedly enhanced accumulation of Doxo-loaded NPs within bone tumors in both mice and dogs bearing OS. Improved efficacy of Pam-functionalized, Doxo-loaded NPs (Pam-Doxo-NPs) was demonstrated in a preclinical orthotopic mouse model of OS. Most importantly, through the inclusion of dogs with naturally developing OS, clinically relevant dosages of Pam-Doxo-NPs could be evaluated for biocompatibility, biodistribution, and anticancer activities in a large mammalian modeling system.

Results

Synthesis and Characterization of Pam-Doxo-NPs. The Pam-Doxo-NPs were constructed through nanoprecipitation of Doxo-PLA polymer conjugates, poly(ethylene glycol)-*b*-PLA (PEG-PLA) and Pam-conjugated PEG-PLA (PLA-PEG-Pam) (Fig. 1A). Doxo-PLA polymer conjugates were synthesized by using the Doxo-initiated ring-opening polymerization (ROP) strategy as described previously (34). This method allowed for quantitative incorporation of Doxo into PLA polymers and resulted in Doxo-PLA conjugates with precisely controlled composition and molecular weights (Fig. 1A). At a monomer/initiator (LA/Doxo) ratio of 10, Doxo loading was achieved as high as 27.4 wt % with nearly 100% incorporation efficiency. Pam was covalently conjugated to PLA-PEG-COOH polymer via stable amide bond as evidenced by ¹H NMR (Fig. 1A and Fig. S1). The resultant Doxo-PLA polymer conjugate was mixed with a mixture of PLA-PEG and PLA-PEG-Pam in dimethylformamide (DMF) followed by nanoprecipitation into rapidly stirred water as nonsolvent to prepare Pam-Doxo-NPs with different Pam contents (Fig. 1B). All of NPs showed similar hydrodynamic sizes (~100 nm) and relatively narrow size distributions (polydispersity index ~0.10) as measured by dynamic light scattering (DLS) (Fig. 1B). NPs with ~100 nm size and narrow size distribution were also evidenced by transmission electron microscopy (TEM) analysis (Fig. 1C). By labeling NPs with radioisotope ⁶⁴Cu [denoted as ⁶⁴Cu-NP, Pam-⁶⁴Cu-NP (10%), and Pam-⁶⁴Cu-NP (50%), respectively] we evaluated the effects of Pam ligand densities on the pharmacokinetic profiles of NPs by monitoring serial blood radioactivity over the course of 24 h. All of the NPs exhibited similar circulation half-lives (Fig. 1D and Fig. S2A).

Doxo was conjugated to PLA polymer through ester linkages and could be released from NPs subjected to hydrolysis of ester bonds in the physiological condition. We conducted release

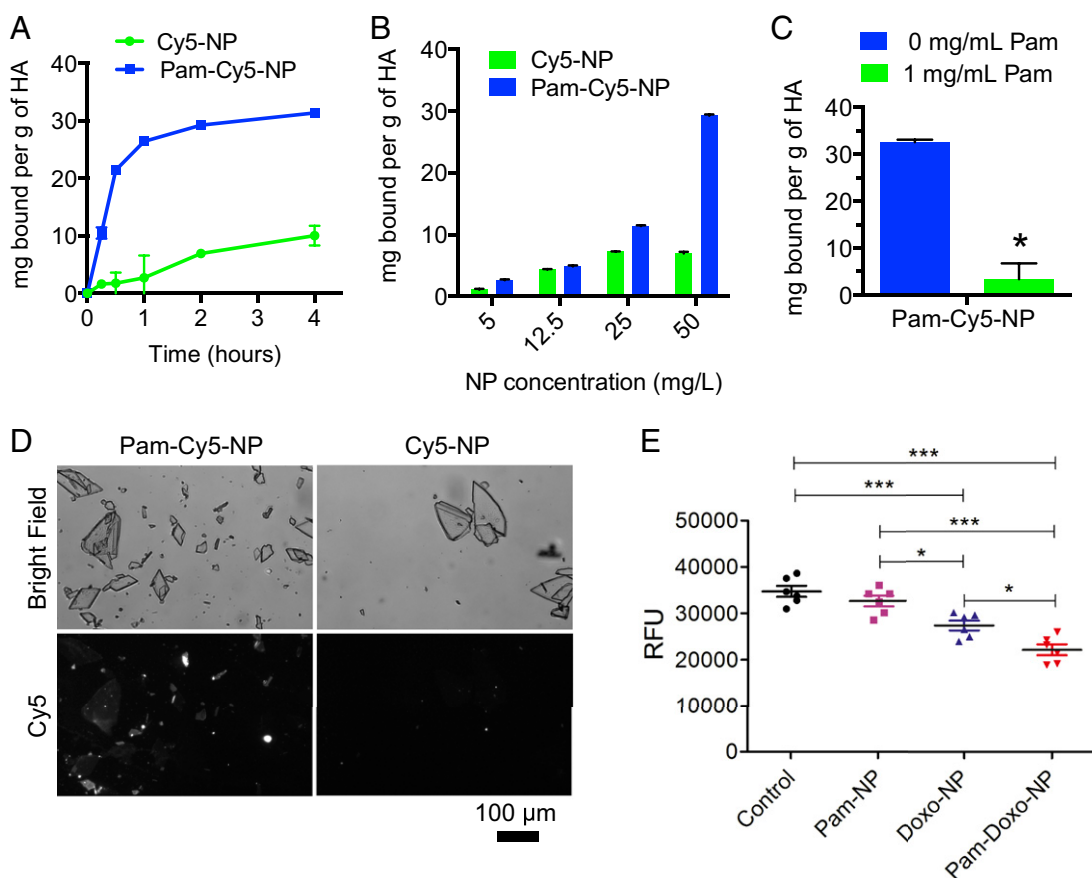


Fig. 2. Binding affinity to HA and cytotoxicity of Pam-Doxo-NPs against GFP-labeled OS cells (K7M2). (A) The kinetics of binding to HA crystals was measured for Cy5-labeled Pam-NPs (Pam-Cy5-NP, solid square) and Cy5-labeled NPs (Cy5-NPs, solid circle). Measurements were acquired at 15 min, 30 min, and 1, 2, and 4 h after mixing. Data presented as average \pm SEM. (B) Steady-state binding to HA crystals was measured for Pam-Cy5-NPs (blue column) and Cy5-NPs (green column) at 2 h. (C) The binding of Pam-Cy5-NPs to HA crystals was measured at 2 h of incubation with (green column) or without (blue column) the existence of free Pam (1 mg/mL). Data presented as average \pm SEM, and analyzed with two-tailed student *t* test; significance defined as **P* < 0.05, ***P* < 0.01, and ****P* < 0.001. (D) Direct visualization of Pam-Cy5-NPs and Cy5-NPs binding to HA using fluorescence microscopy. Bright-field (Top) and Cy5 fluorescence (Bottom) images of HA crystals treated with Pam-Cy5-NPs (50 µg/mL) or Cy5-NPs (50 µg/mL) are shown. (Scale bar: 100 µm.) (E) Differences in K7M2 GFP cell density after 7 d of incubation following 15-min pulse exposure to blank NPs (no Doxo, Pam modified), Doxo-NPs, and Pam-Doxo-NPs (Doxo equivalent dose: 3,000 ng/mL). Untreated cells served as control. Data presented as average relative fluorescence units (RFU) of GFP and analyzed with one-way ANOVA and post hoc Tukey test; significance defined as **P* < 0.05, ***P* < 0.01, and ****P* < 0.001.

kinetic studies of Pam-Doxo-NPs in PBS buffer at pH 5.0 and 7.4. The release kinetics of Doxo from NPs was controllable in a sustained manner without burst release effect at both pH values. The release rate of Doxo from NPs was also pH-dependent, evidenced by accelerated release kinetics at increased acidities, likely due to faster hydrolysis at lower pH (Fig. S2B). Moreover, the Pam-Doxo-NPs could be formulated as a solid form upon lyophilization with human serum albumin as a lyoprotectant. Lyophilized Pam-Doxo-NPs, when reconstituted in buffer solution, maintained original size and narrow particle size distribution (Fig. S2C).

When incubating Pam-Doxo-NPs in 50% (vol %) FBS buffer, Pam-Doxo-NPs (50%) showed a slow time-dependent size increase after 4 d of incubation, whereas Pam-Doxo-NPs (10%) demonstrated more durable maintenance of size without aggregation (Fig. S2D). Considering the stability of NPs as a critical determinant for their *in vivo* biological performance, Pam-Doxo-NPs (10%) were chosen for further live animal exploration.

In Vitro HA Binding Capability and Cytotoxicity of Pam-Doxo-NPs. To characterize the potential bone-binding affinity of Pam-modified NPs, we first performed an *in vitro* HA adsorption assay using Cy5-labeled NPs (Cy5-NPs). HA was considered as an ideal

model substrate because it constitutes the major inorganic component of bone and undergoes erosive osteolysis secondary to the growth of invasive osteotropic solid malignancies. As shown in Fig. 2A, Pam-modified Cy5-NPs (Pam-Cy5-NPs) exhibited rapid and strong binding with HA, with 10.5 mg of Pam-Cy5-NP bound per gram of HA during the first 15 min of incubation and gradually reached equilibrium by 4 h. In contrast, nontargeted Cy5-NPs showed minimal binding capability with HA (1.6 mg of NP bound per gram of HA) during the first 15 min of incubation and exhibited approximately threefold reduced binding capability with HA compared with the Pam-Cy5-NPs over 4 h of incubation. To determine whether the binding of Pam-Cy5-NPs to HA exhibits adsorptive characteristics similar to those of free aminobisphosphonate, we measured the steady-state binding affinity by titrating the concentrations of NPs. The results showed that the binding capacity was proportional to the concentrations of Pam-Cy5-NPs, whereas the Cy5-NPs had a nonspecific adsorption to HA (Fig. 2B). To confirm the binding of Pam-Cy5-NPs with HA was a specific effect of Pam targeting, we conducted a competitive binding experiment in which we preincubated free Pam with HA for 24 h and then measured the binding capacity of Pam-Cy5-NPs with HA after 2 h of incubation, while in the presence of free Pam. The pre- and

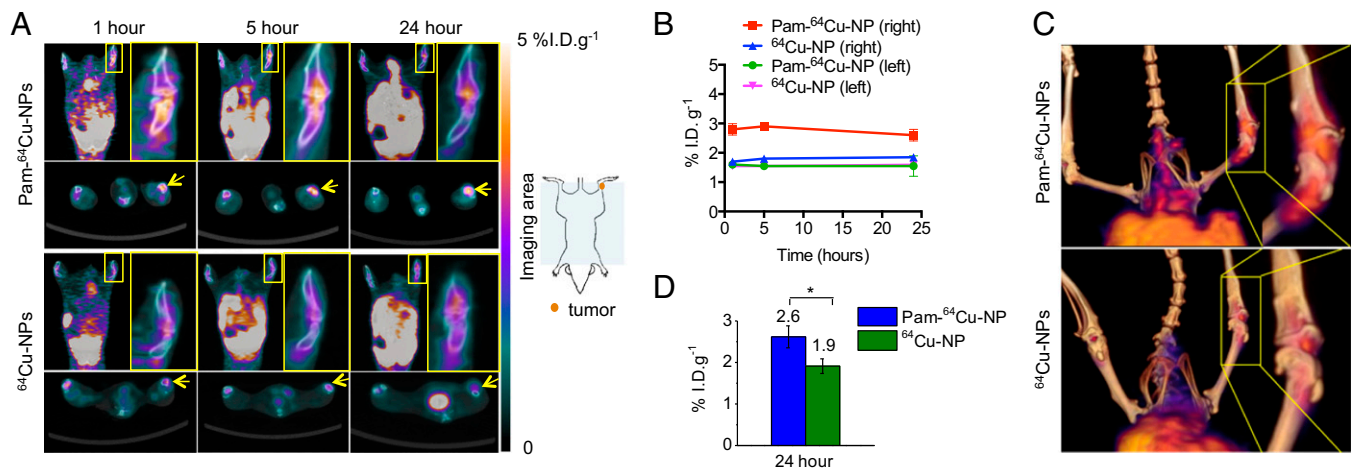


Fig. 3. Radiolabeled Pam-NP improves in vivo intratumoral accumulation in murine orthotropic OS after systemic administration. (A) In vivo whole-body dynamic micro-PET/CT imaging of mice was performed to assess the accumulation of Pam-⁶⁴Cu-NPs and ⁶⁴Cu-NPs in the tumor-residing right hind leg (yellow box and arrow) at 1, 5, and 24 h p.i. (amplified, *Inset* in yellow box). (B) The kinetics of the accumulation of Pam-⁶⁴Cu-NPs and ⁶⁴Cu-NPs in tumor-residing right hind leg and normal contralateral left hind leg at 1, 5, and 24 h p.i., evaluated by micro-PET/CT imaging. Data presented as average \pm SEM. (C) The corresponding 3D micro-PET/CT imaging at 5 h p.i. shows accumulation of Pam-⁶⁴Cu-NPs or ⁶⁴Cu-NPs in the tumor-residing right hind leg (amplified, *Inset*). (D) The accumulation of Pam-⁶⁴Cu-NPs and ⁶⁴Cu-NPs in bone tumor-residing right hind leg, assessed by gamma counter. Data presented as average \pm SEM, and analyzed with two-tailed student *t* test; significance defined as **P* < 0.05, ***P* < 0.01, and ****P* < 0.001.

coincubation of HA with free Pam significantly reduced the binding of Pam-Cy5-NP to HA by 90% (Fig. 2C), indicating that Pam was principally responsible for HA binding. To further characterize the binding of NPs to HA, tandem bright field and fluorescence microscopy were used. With Cy5 fluorescence intensity confirmed to linearly correlate with NP concentration (Fig. S3), Pam-Cy5-NPs consistently adsorbed to exposed surface and edges of the HA crystals, whereas Cy5-NPs only minimally adhered to HA crystals (Fig. 2D).

Given the increased binding capacity of Pam-NPs to HA, we reasoned that Pam-NPs carrying chemotherapeutic agents may exert greater cytotoxicity to tumor cells residing within the bone microenvironment by virtue of their preferential deposition. To investigate this possibility, we evaluated the effect of Pam-Doxo-NPs against GFP-labeled K7M2 OS cells grown on HA-coated culture plates, in which the numbers of viable K7M2 OS cells were directly proportional to GFP fluorescent intensities (Fig. S4). After 7 d of growth, GFP-labeled K7M2 OS cells exhibited the greatest reduction in cell numbers following a 15-min pulse exposure to Pam-Doxo-NPs (Fig. 2E). The results were consistent with the preferential adherence of Pam-Doxo-NPs to HA and consequent prolonged exposure of K7M2 cells to cytotoxic effects of Doxo in vitro.

In Vivo OS Targeting and Efficacy of Pam-Doxo-NPs in Mice. To investigate the in vivo targeting capability of Pam-NPs for osteotropic solid tumors like OS, we next labeled Pam-NPs and nontargeted NPs with ⁶⁴Cu (denoted as Pam-⁶⁴Cu-NP and ⁶⁴Cu-NP, respectively; Fig. S5A), assessed ⁶⁴Cu labeling stability of NPs in serum as a function of time (Fig. S5C), and monitored their biodistribution after i.v. administration into BALB/c mice bearing firefly luciferase transfected K7M3 OS tumors with noninvasive micropositron emission tomography/X-ray computed tomography (micro-PET/CT) imaging (Fig. 3A). In mice, the right hind leg was inoculated with K7M3 cells whereas the normal contralateral left hind leg served as an internal control. Established growth of K7M3 cells within the proximal tibial bone was confirmed using a bioluminescence imaging (BLI) taken at 14 d post-inoculation of the K7M3 cells (Fig. S5B). As shown in Fig. 3A, merged CT and PET images demonstrated noticeable radioactivity in the tumor-bearing right hind leg of a representative

mouse injected with Pam-⁶⁴Cu-NP (2.8% injected dose per gram of tissue (%I.D.g⁻¹) as early as 1 h postinjection (p.i.) (Fig. 3B), whereas in comparison the radioactivity detected in the normal contralateral left hind leg was \sim 50% less (1.6%I.D.g⁻¹). The increased radioactivity detected in the tumor-bearing leg was maintained for as long as 24 h p.i. (2.6%I.D.g⁻¹, Fig. 3B), suggesting the Pam-⁶⁴Cu-NPs were preferentially retained in the osteolytic tumor microenvironment, presumably due to the high binding affinity with inorganic bone matrix. In contrast, the accumulation of nontargeted ⁶⁴Cu-NPs was much lower than that of Pam-⁶⁴Cu-NP (1.7 versus 2.8%I.D.g⁻¹ 1 h p.i. and 1.9 versus 2.6%I.D.g⁻¹ 24 h p.i.) and showed no difference between tumor-bearing right hind legs (1.9%I.D.g⁻¹) and normal contralateral left hind legs (1.6%I.D.g⁻¹) (Fig. 3B). Three-dimensional reconstructed imaging and movies also provide evidence for the significantly enhanced accumulation of Pam-⁶⁴Cu-NPs in the right leg at 5 h p.i. compared with ⁶⁴Cu-NPs (Fig. 3C and Movies S1 and S2). These results were further confirmed by ex vivo measurement of radioactivity 24 h p.i. in surgically resected tumor-bearing right hind legs with a gamma counter (2.6 and 1.9%I.D.g⁻¹ for Pam-⁶⁴Cu-NPs and ⁶⁴Cu-NPs, respectively) (Fig. 3D). The accumulation of Pam-⁶⁴Cu-NPs and ⁶⁴Cu-NPs in the blood and other organs were also assessed by gamma counter and demonstrated comparable soft tissue biodistribution profiles in other organs (Fig. S5D), although Pam-⁶⁴Cu-NPs accumulated to a greater extent within reticuloendothelial organs than nontargeted ⁶⁴Cu-NPs.

Given the preferential accumulation of Pam-NPs to focal regions of skeletal osteolysis demonstrated by micro-PET/CT images, we reasoned that improved antitumor activity could be achieved with Pam-NPs loaded with Doxo. To investigate this therapeutic potential, we evaluated the efficacy of Pam-Doxo-NPs using the K7M3 OS model and a defined treatment protocol (Fig. 4A), in which in vivo tumor burden was demonstrated to be well correlated with the bioluminescent signal intensity (Fig. S6A). Fourteen days following K7M3 inoculation, mice were imaged and equally distributed based upon bioluminescent intensities into four i.v. therapeutic groups (*n* = 6), being saline, Pam functionalized blank vehicles (Pam-NPs), Doxo-NPs, and Pam-Doxo-NPs. Following randomization, mice received i.v. therapy once weekly for two consecutive weeks and were then

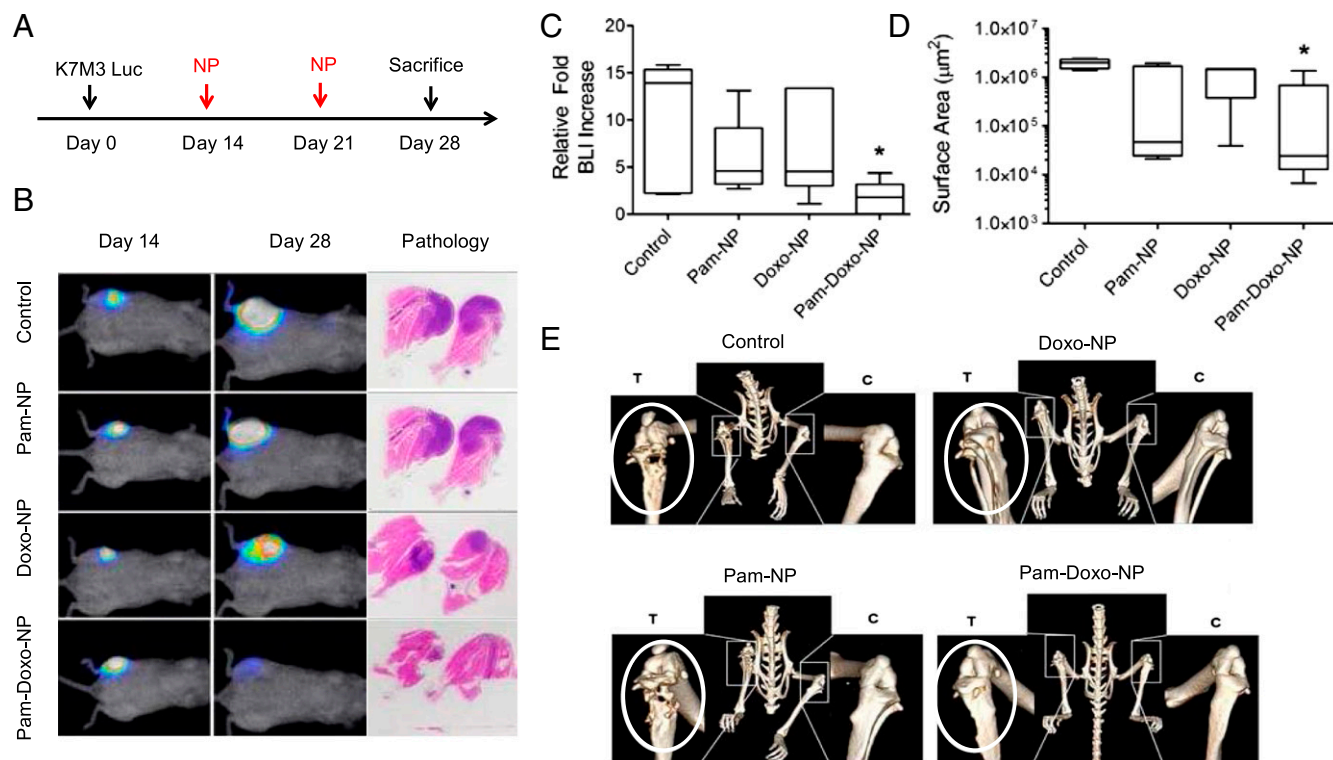


Fig. 4. Pam-Doxo-NPs exert anticancer activities in murine orthotopic OS after systemic administration. (A) Experimental procedure of in vivo bone tumor induction and treatment protocol. (B) Serial changes in K7M3 BLI as a function of time and treatment. Representative bioluminescent signal of mice before treatment and after different treatments, PBS as control, Pam-NP, Doxo-NP, and Pam-Doxo-NP (Doxo equivalent dose: 50 mg/kg), and representative H&E images for pathology analysis. (C and D) The relative tumor burden increase of four groups of mice after treatments, evaluated and quantified by (C) BLI and (D) histopathology. Data expressed as median and interquartile range and compared with Kruskal–Wallis nonparametric ANOVA and post hoc Dunn’s test; significance defined as $*P < 0.05$ comparing with PBS as control. (E) Micro-CT images of proximal tibias [tumor (T) versus control (C)] in four representative mice receiving different i.v. treatments of NPs. White circle indicates the leg with inoculated tumor.

monitored for an additional week before they were killed (Fig. 4A). As expected, mice treated with Pam-Doxo-NPs achieved the greatest delay in localized tumor growth in comparison with all other treatment groups (Fig. 4B–D). Importantly, although Pam-NPs and Doxo-NPs marginally slowed primary tumor growth in comparison with saline-treated mice, only mice receiving Pam-Doxo-NPs had the possibility of achieving macroscopic tumor volume regression, whereas all mice receiving other therapies (saline, Pam-NPs, or Doxo-NPs) uniformly demonstrated tumor progression between days 14 and 28 of study (Fig. 4B and C). The median fold increase of bioluminescent signal from day 14 (pretreatment) following two consecutively weekly treatments of i.v. Pam-Doxo-NPs was 1.8-fold, whereas treatment with saline, Pam-NPs, or Doxo-NPs produced markedly higher median fold increases of bioluminescent signal (13.9-, 4.6-, and 4.5-fold, respectively; Fig. 4C). In addition to bioluminescent signal changes, histologic analysis of tumor surface area postmortem also supported increased anticancer activities exerted by Pam-Doxo-NPs above other treatment groups (Fig. 4B and D). For mice treated with Pam-Doxo-NPs, the median tumor surface area was $2.4 \times 10^4 \mu\text{m}^2$ ($P < 0.05$, compared with saline control); however, no difference in tumor surface area was identified among the remaining three treatment groups (Fig. 4D). To further confirm the enhanced efficacy achieved by Pam-Doxo-NPs, the extent and degree of bone destruction resultant from localized OS progression was evaluated by micro-CT. As illustrated in Fig. 4E, severe pathologic osteolysis associated with OS progression could be readily identified within the right proximal tibias of tumor-bearing mice receiving saline, Pam-NPs, and, to a lesser extent, Doxo-NPs. In contrast, malignant osteolysis

was attenuated in mice receiving Pam-Doxo-NPs and resulted in a trend toward increased percentage of bone volume (leg with K7M3 tumor/normal leg $\times 100\%$) (Fig. S6B). Collectively the observations of reduced bioluminescent signal change and tumor surface area, as well as the trend toward preserved bone volume, provide strong support for increased antitumor efficacy of Pam-Doxo-NPs compared with their nontargeted counterparts in an orthotopic murine model of OS.

Clinical Evaluation of OS Tumor Targeting and Efficacy of Pam-Doxo-NPs in Dogs. Given the promising results in the preclinical murine models, we sought to further test the translational application of Pam-NPs in a large mammalian model system. For these purposes, we chose to use dogs that naturally and spontaneously develop appendicular OS to serve as a physiologically relevant model of focal malignant osteolysis similar to what occurs in human cancer patients. As part of a phase I clinical trial in pet dogs diagnosed with OS, we studied the dynamic in vivo biodistribution profile of i.v. administered Pam-NPs labeled with $^{99\text{m}}\text{Tc}$ in dogs (Fig. S7A). Upon i.v. infusion, Pam-NPs labeled with $^{99\text{m}}\text{Tc}$ were rapidly distributed to all major visceral organs including the heart, kidney, spleen, and liver, with eventual elimination into the urinary bladder (Fig. 5A and B). Importantly, localization and accumulation of $^{99\text{m}}\text{Tc}$ -labeled Pam-NPs was observed within the localized bone tumor microenvironment, indicating that Pam surface modification can quickly target areas of malignant osteolysis in vivo within 1–2 h after administration (Fig. 5C). Furthermore, $^{99\text{m}}\text{Tc}$ activity preferentially intensified in a time-dependent manner, suggesting the dynamic concentration and accumulation of Pam-NPs within

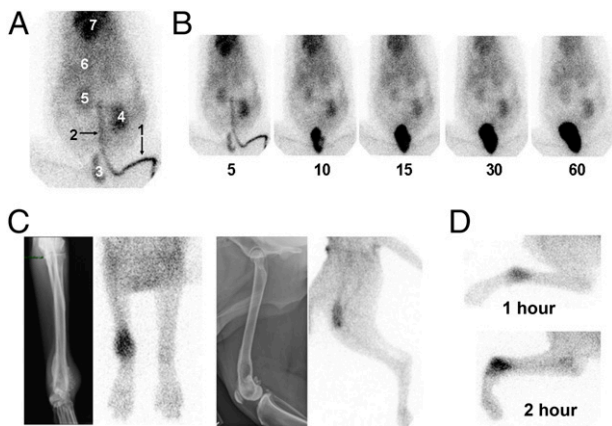


Fig. 5. Biodistribution of ^{99m}Tc -labeled Pam-Doxo-NPs in pet dogs with OS. (A) Dynamic overlay of 180 gamma camera images acquired over 3 min (1 image per s) of ^{99m}Tc -labeled Pam-Doxo-NPs infused i.v. into a pet dog with OS. Tracking of ^{99m}Tc -labeled Pam-Doxo-NPs can be readily observed in highly perfused visceral tissues [1, site of i.v. infusion (lateral saphenous vein); 2, descending caudal vena cava; 3, urinary bladder; 4, left kidney; 5, right kidney; 6, liver; and 7, heart]. (B) Serial images from 5 to 60 min postinfusion of ^{99m}Tc -labeled Pam-Doxo-NPs demonstrates prolonged dwell time in highly vascular visceral organs with ultimate renal elimination into the bladder. (C) In vivo preferential localization of ^{99m}Tc -labeled Pam-Doxo-NPs to regions of focal malignant osteolysis in two representative dogs with OS (Left, dog 1 with distal OS and Right, dog 2 with distal femoral OS) confirmed by colocalization of pathologic radiographic changes and ^{99m}Tc activity. (D) Representative images of progressive ^{99m}Tc -labeled Pam-Doxo-NPs accumulation within focal areas of malignant osteolysis as a function of time (1 and 2 h p.i.).

the bone tumor microenvironment (Fig. 5D). To confirm that the detection of ^{99m}Tc radioactivity by gamma camera in pet dogs with OS was indeed ^{99m}Tc -labeled Pam-NPs and not simply free ^{99m}Tc as a consequence of spontaneous dissociation from Pam-NPs in vivo, we assessed the radiochemical purity of ^{99m}Tc labeled Pam-NPs immediately before i.v. infusion and also the ^{99m}Tc signal

that accumulated in the bladder (urine) 2 h postinfusion (Fig. S7B). The radiochemical purities of ^{99m}Tc -labeled Pam-NPs immediately before i.v. infusion and 2 h postinfusion found within the urine were greater than 95%, providing evidence that the detected ^{99m}Tc radioactivity in pet dogs with OS was indeed associated with ^{99m}Tc -labeled Pam-NPs.

Upon confirming the osteotropic homing properties of Pam-NPs in dogs with OS, we next sought to explore the tolerability and anticancer activities of Pam-Doxo-NPs. Through a rapid dose-escalation protocol (Fig. 6A), nine pet dogs with OS were treated with a single i.v. infusion of Pam-Doxo-NPs, with each subsequent pet dog recruited for study progressively receiving a greater dosage of Doxo equivalent (0–180 mg/m² dose equivalent). Following i.v. infusion, pet dogs were monitored for hematologic and biochemical toxicity weekly for 3 wk and then underwent amputation of the diseased limb to allow for histologic assessment of anticancer activity (percent tumor necrosis) within the primary OS lesion. Even at the highest Doxo dosage equivalent evaluated (180 mg/m²), Pam-Doxo-NPs were safe and did not cause any hematologic, renal, or persistent hepatic toxicity (Fig. 6B and C). In two dogs, mild to moderate elevations in liver transaminases were identified 1 wk following Pam-Doxo-NP administration but trended toward normalization upon subsequent reevaluations. In addition to hematologic and biochemical tolerability of Pam-Doxo-NP, no evidence of cardiotoxicity was identified in any dog as determined by circulating cardiac troponin-I concentrations (Fig. S8). In addition, Pam-Doxo-NPs exerted moderate anticancer activity as determined by percent tumor necrosis, which was correlated ($r^2 = 0.61$, $P = 0.04$) with three factors that dictated the concentrations of Doxo achieved within the bone tumor microenvironment: (i) total dosage of Doxo, (ii) magnitude of ^{99m}Tc -labeled Pam-Doxo-NPs accumulation within the tumor site, and (iii) overall bone tumor volume of distribution (Fig. 7).

Discussion

The past several decades have witnessed the explosive development of nanomedicine, and the combination of nanotechnology

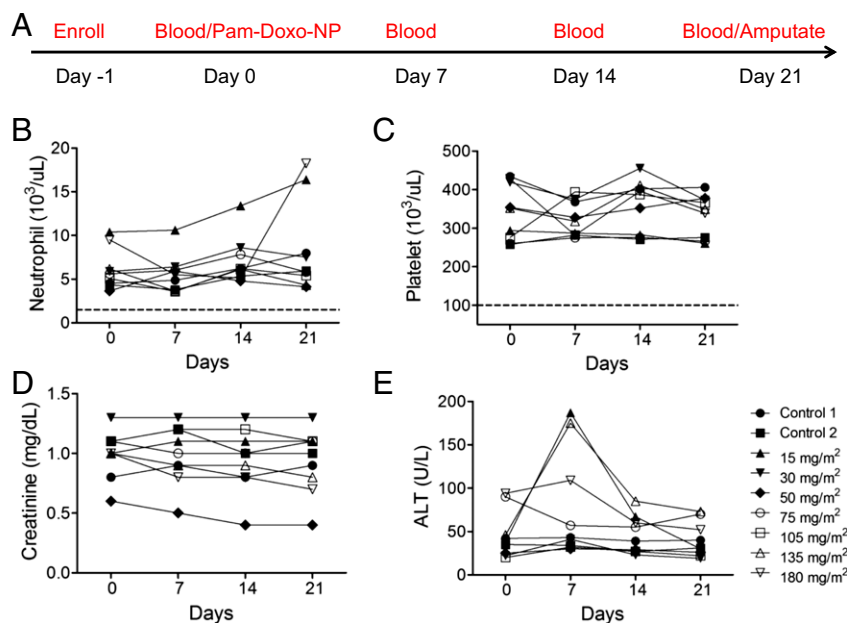


Fig. 6. Exceptional biocompatibility of Pam-Doxo-NPs following single-dose i.v. infusion. (A) Clinical trial design for pet dogs receiving Pam-Doxo-NPs. (B) Hematologic and (C) biochemical safety profile of Pam-Doxo-NPs following single-dose, i.v. administration. Complete absence of grade I toxicity (dotted line) for total neutrophil and platelet counts throughout entirety of study. (D) Complete absence of renal toxicity as assessed by serum creatinine, and (E) mild and transient elevations in liver transaminases identified 1 wk p.i. of Pam-Doxo-NPs administration in minority of pet dogs treated.

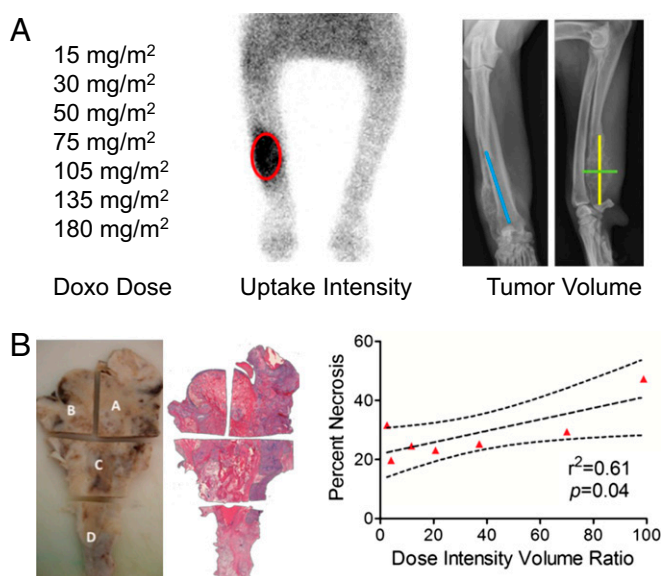


Fig. 7. Anticancer activities of Pam-Doxo-NPs following single-dose i.v. infusion in pet dogs. (A) Variables that influence anticancer activities exerted by Pam-Doxo-NPs include absolute Doxo dose, ^{99m}Tc-labeling intensity (red oval), and absolute tumor volume [calculated by ellipsoid formula $4/3\pi(\text{length} \times \text{width} \times \text{depth})$]. Primary tumor measurements denoted by colored lines: blue, length; green, width; and yellow, depth. (B) Percent tumor necrosis of bone tumors from amputated dog legs evaluated by H&E staining and linear correlation with the ratio of three variables: (Doxo dose \times ^{99m}Tc-labeling intensity)/(absolute tumor volume). Data analyzed with Pearson correlation; significance defined as $P < 0.05$.

and medicine has brought great promise for the improved treatment of cancer. Compared with conventional chemotherapy, the use of NPs to administer therapeutic agents to tumor tissues could potentially increase targeted drug delivery to tumor cells and the associated microenvironment while reducing the likelihood of adverse side effects, and thus enhancing therapeutic indices (16, 35). Despite these potential advantages, the clinical maturation of nanomedicine from bench to bed has proved very difficult, with fewer than five agents being approved for the treatment of cancer patients (36). One barrier toward the translation of nanomedicine discoveries into medical breakthroughs is the difficulty in identifying optimal physicochemical properties of NPs that will predictably and consistently prolong the in vivo circulation, facilitate intratumoral accumulation, and release drugs in a controlled manner yet simultaneously possess properties that are robustly biocompatible. By uniquely integrating the controlled ROP into the formulation of NPs as described in the present investigation we demonstrated the feasibility of facile large-scale production (up to gram) of highly biocompatible NPs with well-controlled properties of distinct size, narrow size distributions, high drug loading, and sustained drug release profiles (34). Compared with the conventional encapsulation method, this strategy allows for nearly 100% drug incorporation efficiency, and thus precisely controlled drug loadings, only by adjusting monomer/initiator (LA/Doxo) ratios. Furthermore, we successfully demonstrated the developed NPs could be maintained stably as a solid formulation with absolutely no aggregation after reconstitution, a property that can be beneficial for large-scale translational applications.

By taking advantage of the EPR effect, NPs can extravasate through the leaky blood vasculature, accumulate in the tumor tissues, and release their payload sustainably (37). This passive targeting process is largely dependent on the physicochemical properties of NPs (38), and the addition of active targeting

strategies is expected to improve localized drug delivery (39). In this study, we sought to actively target NPs to regions of malignant bone resorption through the use of Pam, a potent aminobisphosphonate used for the treatment of diverse skeletal pathologies (40). The bone microenvironment serves as a fertile “soil” for the dissemination of various solid cancers known as skeletal metastases (41, 42) and serves as the developmental origin for primary bone tumors such as OS and Ewing’s sarcoma (43). As a consequence of osteotropic cancer progression, a large majority of cancer patients afflicted with focal or multifocal skeletal tumors will endure excruciating pain and suffering consequent to uncontrolled malignant bone resorption. As such, there is clinical justification for developing targeted treatment strategies aimed at improving the management of malignant osteolytic syndromes. In the present study, we successfully demonstrated Pam surface-modified PLA NPs could significantly improve their accumulation and retention within the diseased bone tumor microenvironment. Although some data derived from our study suggested increased reticuloendothelial cell uptake of Pam surface modified PLA NPs, which could be the result of Pam serving as a phosphoantigen, no overt toxicities were associated with this effect. Importantly, by virtue of preferential anatomic targeting to the bone microenvironment, Pam-Doxo-NPs were capable of minimizing systemic off-target toxicities and concurrently enhancing localized antitumor activities in not only a preclinical murine tumor model but also in a clinically relevant, large mammalian tumor model, pet dogs with OS.

OS is the most common primary bone tumor diagnosed in pediatric patients and pet dogs, and clinical symptomology includes pain and lameness consequent to localized tumor growth and secondary bone destruction. The clinical presentation, biologic behavior, and genetics of OS are strongly conserved between humans and pet dogs (26, 28, 29, 44), and canine OS has emerged as a powerful comparative tumor model for guiding and expediting the drug development pathway for pediatric OS patients (45, 46). One of the critical factors that contribute to the future clinical translation of nanomedicine is the experimental models used for evaluating the safety and efficiency of targeted NP treatment strategies. Uniquely, in our investigation we not only have incorporated the use of a traditional preclinical murine tumor model of focal bone cancer but also have extended our studies into pet dogs with OS. This population of pet dogs, which develop cancer spontaneously, as do human beings, can serve as a rich and valuable scientific resource for studying osteotropic NP therapies given the comparable skeletal size, metabolism, and physiology shared between pet dogs and people.

The successful safety and anticancer activities reported in the current study in not only murine but also canine model systems are highly significant and provide foundational evidence for the translational impact of the work described. Of noteworthy mention was the exceptional biocompatibility of our NPs; the absolute quantities of NPs infused i.v. into pet dogs was in the gram scale range (up to 2 g), which was over three orders of magnitude greater than those administered to experimental mice. The remarkable safety profile of our reported NP formulation, coupled with its demonstrated activity, provides powerful impetus for its continued development as a novel adjuvant treatment for improving the management of focal and multifocal malignant osteolysis encountered in human cancer patients.

Materials and Methods

Detailed materials and methods are provided [SI Materials and Methods](#). The study protocol was reviewed and approved by the Illinois Institutional Animal Care and Use Committee (IACUC) of the University of Illinois at Urbana Champaign. Dogs with spontaneously occurring appendicular OS were recruited to participate in the present investigational trial conducted at the University of Illinois Veterinary Teaching Hospital to evaluate the

biodistribution, safety, and anticancer activity of Pam-Doxo-NP. Pet owners were informed of all treatment options available for their pet dogs and required to sign client consent forms before their dogs were treated with Pam-Doxo-NP. The study protocol was reviewed and approved by the Illinois IACUC of the University of Illinois at Urbana-Champaign.

Preparation and Characterization of Pam-Doxo-NPs. Doxo-PLA conjugates were synthesized with feeding ratio of lactide/Doxo = 10/1 by following similar procedures as published (34). PLA-PEG-Pam conjugate was synthesized by covalently conjugating Pam to PLA-PEG_{5k}-COOH polymer via stable amide bond (Fig. S1). One hundred-microliter DMF solution of Doxo-PLA (10 mg/mL) was mixed with 100- μ L DMF solution of mixture of PLA-PEG_{5k} (10 mg/mL)/PLA-PEG_{5k}-Pam conjugate (10 mg/mL) at varying ratios and then added dropwise to rapidly stirred nanopure water (4 mL). The resulting Doxo-loaded PLA-PEG-Pam NPs (Pam-Doxo-NPs) with different Pam contents were collected by ultrafiltration [5 min, 3,000 \times g, Ultracel membrane with 10,000 nominal molecular weight limit (NMWL); Millipore], washed with water, and then characterized by DLS for particle sizes and size distributions and by HPLC for drug loadings by following the reported procedures (34). Pam-Doxo-NPs (10%) were chosen for the most *in vitro* and *in vivo* studies unless specified.

In Vitro HA Binding Evaluation. To evaluate the binding kinetics of HA with NPs, 50 μ g/mL Pam-Cy5-NPs or Cy5-NPs in 20-mL deionized (DI) water containing HA (0.75 mg/mL) was continuously stirred at 550 rpm at 37 °C. At different time points, an aliquot of 200 μ L was diluted with 1.0 mL DI water then centrifuged at 1,000 \times g for 5 min to remove the HA and bound NPs. The NP concentration in the supernatant was quantified by measuring the Cy5 fluorescence intensity (15 min, 30 min, and 1, 2, and 4 h) and calculated by standard curve. Bound NPs were calculated by subtracting unbound NPs from the total NPs. To measure the dose-dependent binding, the indicated concentrations of NPs were incubated in 1-mL DI water containing HA (0.75 mg/mL). Suspensions were continuously vortexed at 37 °C for 2 h and the bounded NPs were calculated following the same procedure. In an inhibition study, HA (3 mg/mL) was suspended in PBS with/without free Pam (1 mg/mL) at 37 °C for 24 h. To measure the inhibition effect of free Pam on Pam-Cy5-NPs binding with HA crystals, the Cy5-NPs and Pam-Cy5-NPs solutions (40 μ g/mL) were incubated in PBS (2 mL) containing HA (0.75 mg/mL). Suspensions were stirred at 37 °C for 2 h. An aliquot of 300 μ L was diluted with 900 μ L PBS and then centrifuged at 1,000 \times g for 5 min to remove HA crystals and bound NPs. The NP concentration in the supernatant was quantified by measuring the Cy5 fluorescence intensity and calculated by standard curve. For direct visualization of NPs binding with HA crystals, 50 μ g/mL Pam-Cy5-NPs or Cy5-NPs in 10 mL DI water containing HA (0.75 mg/mL) was incubated at 37 °C for 30 min with continuous vortexing. Crystals were collected and washed with DI water twice, mounted on glass slides, and evaluated using a Zeiss Axiovert 40 CFL fluorescence microscope equipped with a 10 \times objective.

In Vitro Cytotoxicity Evaluation. To evaluate whether prolonged retention of NPs on HA matrix could affect cytotoxicity, K7M2 transfected with GFP, provided by Chand Khanna, National Cancer Institute, Bethesda, were seeded in BD Biotek Osteologic 24-well plates at 10,000 cells per 3 mL of complete media. Upon K7M2 adhesion, cells were exposed to a 15-min pulse of saline (control), Pam-NP, Doxo-NP, or Pam-Doxo-NP with gentle rocking. Following treatment exposure, residual media was removed and replaced with fresh complete media, and K7M2 GFP cells were allowed to grow for an additional 7 d before being lysed and resultant supernatant fluorescent intensities determined with a fluorometric plate reader.

Orthotopic OS Tumor Model. The tumor model was established in 8-wk-old female BALB/c mice by injection of 1×10^6 of firefly luciferase transfected murine OS K7M3 cells, provided by Su Young Kim, National Cancer Institute, Bethesda, suspended in 10 μ L HBSS into the right proximal tibia using an insulin syringe with 1/2-inch, 29-gauge, nondetachable needle. Tumor progression was evaluated using a BLI system (Stanford Photonics) with a dual microchannel plate intensified CCD camera. Each mouse was intraperitoneally injected with a D-luciferin potassium salt solution (0.15 g/kg body weight) 3 min before imaging and then anesthetized with a constant flow of isoflurane-containing oxygen. A gray-scale image of the mouse was first recorded with dimmed light. Photon emission was then integrated for 10 s using the imaging software Piper Control (Stanford Photonics) and visualized in pseudocolor. To localize bioluminescent signals that indicated luciferase-engineered K7M3 tumors, gray-scale images of mouse body and bioluminescent signals of primary tumors were merged using Image J (NIH) and Photoshop Elements (Adobe Systems).

Micro-PET/CT Imaging Evaluation. Female BALB/c mice were inoculated with K7M3-luciferase murine OS cells and primary tumors were allowed to develop over the course of 21 d. Mice were divided into two groups ($n = 4$) and were treated with Pam-⁶⁴Cu-NPs or ⁶⁴Cu-NPs at a dose of 75 μ Ci *i.v.* Mice were placed on the micro-CT imaging bed and kept anesthetized with a constant isoflurane flow. A dynamic PET scan was acquired for 1 h (60-min acquisition time, reconstructed as 60 frames at 60 s per frame). The micro-CT scan (80 keV/500 μ A X-rays energy, 360 projections, 360°, 75- μ m pixel size) was used for determining the anatomical localization of the tumor. Static micro-PET scans were acquired at two selected time points (5 and 24 h *p.i.*) together with micro-CT scans for anatomical coregistration. The obtained micro-PET and micro-CT images were constructed using ordered subset expectation maximization and cone-beam algorithms with existing commercial software (Inveon Acquisition Workspace and Cobra Exxim, respectively). Micro-PET images were processed using 3D median filtering and fused with micro-CT images. To quantify the radioactivity of ⁶⁴Cu in the tumors, complex irregular volumes of interest (VOIs) were drawn on the micro-CT images and registered with micro-PET images to determine mean counts in each VOI. The radiotracer activity from each VOI was normalized by injected dose and expressed at percent of the decay-corrected injected activity per cubic centimeter of tissue, which can be approximated as percentage % I.D. g⁻¹ assuming the density of the tissue is around 1g/cm³. The initial total injected activity was determined by dose calibrator before injection.

In Vivo Biodistribution Evaluation with Gamma Counter. Female BALB/c mice bearing K7M3-luciferase murine OS cells were allowed to develop primary bone tumors over 21 d and then were divided into two groups ($n = 4$), minimizing the weight differences. The two groups of mice were treated with Pam-⁶⁴Cu-NPs or ⁶⁴Cu-NPs at a dose of 75 μ Ci *i.v.* Mice were killed 24 h *p.i.* The blood and major organs (liver, spleen, kidney, heart, lung, intestine, and bladder) as well as K7M3 tumors containing right leg and normal left leg were collected, weighed, and measured for radioactivity (⁶⁴Cu) with a gamma counter (Wizard2; PerkinElmer) using an appropriate energy window centered at photo peak of 511 keV. Raw counts were corrected for background, decay, and weight. Corrected counts were converted to microcurie per gram of tissue with a previously determined calibration curve by counting the ⁶⁴Cu standards. The activity in blood and each collected tissue sample was calculated as percentage of the injected dose per gram of tissue (% I.D. g⁻¹). For this calculation, the tissue radioactivity was corrected for the ⁶⁴Cu decay [T(1/2) = 12.7 h] to the time of gamma-well counting.

In Vivo Anticancer Efficacy Evaluation Using Murine Orthotopic OS Tumor Model. Female BALB/c mice inoculated with K7M3-luciferase murine OS cells were divided into four equivalent groups ($n = 7$) based upon primary tumor burden (BLI) and body weight. Two groups of mice were treated with Pam-Doxo-NPs and Doxo-NPs at a dose of 50 mg/kg (Doxo equivalent) *i.v.* for two consecutive treatments 1 wk apart. The other two groups of mice were treated with blank NPs (no Doxo) and saline as controls. Tumor progression was evaluated using a BLI system (Stanford Photonics) as mentioned above. At the end of the study, mice were killed by CO₂. To ensure complete collection off the right tibia and fibula, the distal femur and talus were incubated in the dissected samples, as well as the surrounding soft tissues. Tissues were placed in 10% (vol/vol) formalin and scanned with micro-CT (80 keV/500 μ A X-rays energy, 360 projections, 360°, 75- μ m pixel size) to determine the bone destruction. After 48 h in 10% (vol/vol) formalin, hind limbs were placed in 10% (wt/wt) EDTA for 7 d to decalcify. All tissues were processed into paraffin and stained with H&E and then evaluated by an experienced pathologist and tumor surface area was quantified by ImageJ software.

In Vivo Biodistribution, Biocompatibility, and Anticancer Efficacy Evaluation Using Spontaneous Canine OS Tumor Model. Treatment naïve dogs with confirmed appendicular OS were recruited to participate in a rapid dose-escalation study evaluating the biodistribution, biocompatibility, and anticancer activities of Pam-Doxo-NPs. For biodistribution studies, Pam-Doxo-NPs were labeled with ^{99m}Tc using a previously reported method (47) and subsequently infused *i.v.* as a 30-min constant-rate infusion into dogs sedated with intramuscular butorphanol and medetomidine. At the time of infusing ^{99m}Tc-labeled Pam-Doxo-NPs, sequential images were acquired every second for 180 s, every 5 min for 1 h, and at 2 h post-infusion. Studies determining the radiochemical purity of ^{99m}Tc-labeled Pam-Doxo-NPs pre- and postinfusion (urine) were performed using a previously described protocol (48). Upon the completion of infusion, the

biocompatibilities of Pam-Doxo-NPs in treated pet dogs were characterized weekly for three consecutive weeks through the conductance of serial physical examination, complete blood count, serum chemistry profiles, and cardiac troponin concentrations. The direct anticancer activities of Pam-Doxo-NPs were evaluated in pet dogs by amputating the OS-affected leg with consequent percent tumor necrosis assessment by histopathologic methods (49). Briefly, the bone and associated tumor were sectioned longitudinally either proximal to distal or lateral to medial dependent on the orientation of the mass lesion. Sections were fixed in formalin for 24–48 h followed by decalcification in an EDTA/HCL decalcifying solution (Richard Allen Scientific). Following decalcification, transverse sections of the longitudinal section were made to allow for placement into large tissue cassettes and sectioning onto glass slides. The sections were processed with an extended protocol, paraffin-embedded, sectioned at 4 μm , and stained with H&E. All slides (microscopic specimens), which cumulatively represent the entire plane in which the gross specimen was sectioned, were scanned in their entirety using an AxioCam HRc Carl Zeiss camera coupled to a Carl Zeiss Axioplan 2 microscope with a mechanical stage and using Carl Zeiss KS 400 analysis software. The scanned images were viewed in Adobe Photoshop CS3 (Adobe Systems) to allow image analysis of tumor necrosis, and the original glass slides of the

corresponding section were simultaneously viewed via light microscopy (Olympus BX41), providing detailed assessment of regions isolated on the digitally scanned images. Using Adobe Photoshop software and the scanned images, the total tumor area and regions of tumor necrosis were outlined in two different outlining colors. Regions outlined on the images were analyzed with the Carl Zeiss KS 400 image analysis software to quantitate total tumor area and the area of tumor necrosis. Ultimately, the overall total tumor area and total area of tumor necrosis for a given tumor were determined by adding the results (values) of each respective section. Percent necrosis for individual tumors was calculated as total area of necrosis/total tumor area.

ACKNOWLEDGMENTS. This work was supported by Morris Animal Foundation for the conductance of the phase I dose-escalation study in pet dogs with osteosarcoma, Grant D09CA-083 (to T.M.F.); NIH Director's New Innovator Award Program Grant 1DP2OD007246-01, which supported in vitro and in vivo studies, and National Science Foundation Division of Materials Research Grant 1309525, which supported the synthesis of materials (both to J.C.); and NIH National Cancer Institute Alliance for Nanotechnology in Cancer "Midwest Cancer Nanotechnology Training Centre" Grant R25 CA154015A (to Q.Y., L.T., and K.C.).

- Mukherjee D, et al. (2011) Survival of patients with malignant primary osseous spinal neoplasms: Results from the Surveillance, Epidemiology, and End Results (SEER) database from 1973 to 2003. *J Neurosurg Spine* 14(2):143–150.
- Hirsh V (2009) Skeletal disease contributes substantially to morbidity and mortality in patients with lung cancer. *Clin Lung Cancer* 10(4):223–229.
- Coleman RE (1997) Skeletal complications of malignancy. *Cancer* 80(8, Suppl):1588–1594.
- Mantyh P (2013) Bone cancer pain: Causes, consequences, and therapeutic opportunities. *Pain* 154(Suppl 1):S54–S62.
- Smith HS, Barkin RL (2014) Painful boney metastases. *Am J Ther* 21(2):106–130.
- Sabino MA, et al. (2003) Different tumors in bone each give rise to a distinct pattern of skeletal destruction, bone cancer-related pain behaviors and neurochemical changes in the central nervous system. *Int J Cancer* 104(5):550–558.
- Frassica DA (2003) General principles of external beam radiation therapy for skeletal metastases. *Clin Orthop Relat Res* (415, Suppl):S158–S164.
- Vakaet LA, Boterberg T (2004) Pain control by ionizing radiation of bone metastasis. *Int J Dev Biol* 48(5-6):599–606.
- Goblirsch M, et al. (2005) Radiation treatment decreases bone cancer pain through direct effect on tumor cells. *Radiat Res* 164(4 Pt 1):400–408.
- Goblirsch M, et al. (2004) Radiation treatment decreases bone cancer pain, osteolysis and tumor size. *Radiat Res* 161(2):228–234.
- Coleman RE (2001) Metastatic bone disease: Clinical features, pathophysiology and treatment strategies. *Cancer Treat Rev* 27(3):165–176.
- Clark JC, Dass CR, Choong PF (2008) Current and future treatments of bone metastases. *Expert Opin Emerg Drugs* 13(4):609–627.
- Coleman RE (2006) Clinical features of metastatic bone disease and risk of skeletal morbidity. *Clin Cancer Res* 12(20 Pt 2):6243s–6249s.
- Weilbaeher KN, Guise TA, McCauley LK (2011) Cancer to bone: A fatal attraction. *Nat Rev Cancer* 11(6):411–425.
- Wang D, Miller SC, Kopecková P, Kopecek J (2005) Bone-targeting macromolecular therapeutics. *Adv Drug Deliv Rev* 57(7):1049–1076.
- Davis ME, Chen ZG, Shin DM (2008) Nanoparticle therapeutics: An emerging treatment modality for cancer. *Nat Rev Drug Discov* 7(9):771–782.
- Choi CHJ, Alabi CA, Webster P, Davis ME (2010) Mechanism of active targeting in solid tumors with transferrin-containing gold nanoparticles. *Proc Natl Acad Sci USA* 107(3):1235–1240.
- Byrne JD, Betancourt T, Brannon-Peppas L (2008) Active targeting schemes for nanoparticle systems in cancer therapeutics. *Adv Drug Deliv Rev* 60(15):1615–1626.
- Pignatello R, et al. (2009) A novel biomaterial for osteotropic drug nanocarriers: Synthesis and biocompatibility evaluation of a PLGA-ALE conjugate. *Nanomedicine (Lond)* 4(2):161–175.
- Choi SW, Kim JH (2007) Design of surface-modified poly(D,L-lactide-co-glycolide) nanoparticles for targeted drug delivery to bone. *J Control Release* 122(1):24–30.
- Morton SW, et al. (2014) Osteotropic therapy via targeted layer-by-layer nanoparticles. *Adv Health Mater* 3(6):867–875.
- Swami A, et al. (2014) Engineered nanomedicine for myeloma and bone microenvironment targeting. *Proc Natl Acad Sci USA* 111(28):10287–10292.
- Ottaviani G, Jaffe N (2009) The epidemiology of osteosarcoma. *Cancer Treat Res* 152:3–13.
- Fenger JM, London CA, Kisseberth WC (2014) Canine osteosarcoma: A naturally occurring disease to inform pediatric oncology. *ILAR J* 55(1):69–85.
- Withrow SJ, Khanna C (2009) Bridging the gap between experimental animals and humans in osteosarcoma. *Cancer Treat Res* 152:439–446.
- Paoloni M, et al. (2009) Canine tumor cross-species genomics uncovers targets linked to osteosarcoma progression. *BMC Genomics* 10:625.
- Rankin KS, et al. (2012) Of dogs and men: Comparative biology as a tool for the discovery of novel biomarkers and drug development targets in osteosarcoma. *Pediatr Blood Cancer* 58(3):327–333.
- Angstadt AY, et al. (2011) Characterization of canine osteosarcoma by array comparative genomic hybridization and RT-qPCR: Signatures of genomic imbalance in canine osteosarcoma parallel the human counterpart. *Genes Chromosomes Cancer* 50(11):859–874.
- Angstadt AY, Thayanithy V, Subramanian S, Modiano JF, Breen M (2012) A genome-wide approach to comparative oncology: High-resolution oligonucleotide aCGH of canine and human osteosarcoma pinpoints shared microaberrations. *Cancer Genet* 205(11):572–587.
- London CA, et al. (2011) Phase I evaluation of STA-1474, a prodrug of the novel HSP90 inhibitor ganetespib, in dogs with spontaneous cancer. *PLoS One* 6(11):e27018.
- London CA, et al. (2014) Preclinical evaluation of the novel, orally bioavailable Selective Inhibitor of Nuclear Export (SINE) KPT-335 in spontaneous canine cancer: results of a phase I study. *PLoS One* 9(2):e87585.
- Maeda H, Nakamura H, Fang J (2013) The EPR effect for macromolecular drug delivery to solid tumors: Improvement of tumor uptake, lowering of systemic toxicity, and distinct tumor imaging in vivo. *Adv Drug Deliv Rev* 65(1):71–79.
- Prabhakar U, et al. (2013) Challenges and key considerations of the enhanced permeability and retention effect for nanomedicine drug delivery in oncology. *Cancer Res* 73(8):2412–2417.
- Tong R, Cheng J (2009) Ring-opening polymerization-mediated controlled formulation of polylactide-drug nanoparticles. *J Am Chem Soc* 131(13):4744–4754.
- Egusquiguire SP, Igartua M, Hernández RM, Pedraz JL (2012) Nanoparticle delivery systems for cancer therapy: Advances in clinical and preclinical research. *Clin Transl Oncol* 14(2):83–93.
- Venditto VJ, Szoka FC, Jr (2013) Cancer nanomedicines: So many papers and so few drugs! *Adv Drug Deliv Rev* 65(1):80–88.
- Greish K (2007) Enhanced permeability and retention of macromolecular drugs in solid tumors: A royal gate for targeted anticancer nanomedicines. *J Drug Target* 15(7-8):457–464.
- Tang L, et al. (2014) Investigating the optimal size of anticancer nanomedicine. *Proc Natl Acad Sci USA* 111(43):15344–15349.
- Bertrand N, Wu J, Xu X, Kamaly N, Farokhzad OC (2014) Cancer nanotechnology: The impact of passive and active targeting in the era of modern cancer biology. *Adv Drug Deliv Rev* 66:2–25.
- Fitton A, McTavish D (1991) Pamidronate. A review of its pharmacological properties and therapeutic efficacy in resorptive bone disease. *Drugs* 41(2):289–318.
- Mundy GR (2002) Metastasis to bone: Causes, consequences and therapeutic opportunities. *Nat Rev Cancer* 2(8):584–593.
- Suva LJ, Washam C, Nicholas RW, Griffin RJ (2011) Bone metastasis: Mechanisms and therapeutic opportunities. *Nat Rev Endocrinol* 7(4):208–218.
- van Driel M and van Leeuwen JPTM (2014) Cancer and bone: A complex complex. *Arch Biochem Biophys* 561:159–166.
- Withrow SJ, Powers BE, Straw RC, Wilkins RM (1991) Comparative aspects of osteosarcoma. Dog versus man. *Clin Orthop Relat Res* (270):159–168.
- Khanna C, et al. (2014) Toward a drug development path that targets metastatic progression in osteosarcoma. *Clin Cancer Res* 20(16):4200–4209.
- Paoloni M, Khanna C (2008) Translation of new cancer treatments from pet dogs to humans. *Nat Rev Cancer* 8(2):147–156.
- Kumar V, Kumar D, Howman-Giles RB, Little DG (2007) Is (99m)Tc-labeled pamidronate a better agent than (99m)Tc-medronate for bone imaging? *Nucl Med Commun* 28(2):101–107.
- Sanada S, Ando A, Ando I, Hiraki T, Hisada K (1986) A single-strip mini-paper chromatographic method for rapid purity-control of 99mTc-labeled radiopharmaceuticals. *Eur J Nucl Med* 12(8):390–393.
- Powers BE, et al. (1991) Percent tumor necrosis as a predictor of treatment response in canine osteosarcoma. *Cancer* 67(1):126–134.
- Tong R, et al. (2010) Polylactide nanoparticles containing stably incorporated cyanine dyes for in vitro and in vivo imaging applications. *Microsc Res Tech* 73(9):901–909.